HYDROTHERMAL REPLACEMENT OF BIOGENIC AND ABIOGENIC ARAGONITE BY MG-CARBONATES – RELATION BETWEEN TEXTURAL CONTROL ON EFFECTIVE ELEMENT FLUXES AND RESULTING CARBONATE PHASE

Laura Jonas[a], Thomas Müller[a,b,*], Ralf Dohmen[a], Adrian Immenhauser[a], and Benita Putlitz[c]

[a]Institut für Geologie, Mineralogie und Geophysik, Ruhr-Universität Bochum, Universitätsstrasse 150, D-44801 Bochum, Germany

[b]Institute of Geophysics and Tectonics, School of Earth and Environmental Sciences, University of Leeds, Leeds LS2 9JT, United Kingdom

[c]Institute of Earth Science, University of Lausanne, Geopolis Building, CH-1015 Lausanne, Switzerland

*Corresponding author. Tel.: +44 113 34-31156; Email address: t.mueller@leeds.ac.uk

Abstract

Dolomitization, i.e., the secondary replacement of calcite or aragonite ($CaCO_3$) by dolomite ($CaMg[CO_3]_2$), is one of the most volumetrically important carbonate diagenetic processes. It occurs under near surface and shallow burial conditions and can significantly modify rock properties through changes in porosity and permeability. Dolomitization fronts are directly coupled to fluid pathways, which may be related to the initial porosity/permeability of the precursor limestone, an existing fault network or secondary porosity/permeability created through the replacement reaction. In this study, the textural control on the replacement of biogenic and abiogenic aragonite by Mg-carbonates, that are typical precursor phases in the dolomitization process, was experimentally studied under hydrothermal conditions. Aragonite samples with different textural and microstructural properties exhibiting a compact (inorganic aragonite single crystal), an intermediate (bivalve shell of Arctica islandica) and open porous structure (skeleton of coral Porites sp.) were reacted with a solution of 0.9 M $MgCl_2$ and 0.015 M $SrCl_2$ at 200 °C. The replacement of aragonite by a Ca-bearing magnesite and a Mg-Ca carbonate of non-stoichiometric dolomitic composition takes place via a dissolution-precipitation process

and leads to the formation of a porous reaction front that progressively replaces the aragonite precursor. The reaction leads to the development of porosity within the reaction front and distinctive microstructures such as gaps and cavities at the reaction interface. The newly formed reaction rim consists of chemically distinct phases separated by sharp boundaries. It was found that the number of phases and their chemical variation decreases with increasing initial porosity and reactive surface area. This observation is explained by variations in effective element fluxes that result in differential chemical gradients in the fluid within the pore space of the reaction rim. Observed reaction rates are highest for the replacement of the initially highly porous coral and lowest for the compact structure of a single aragonite crystal. Therefore, the reaction progress equally depends on effective element fluxes between the fluid at the reaction interface and the bulk solution surrounding the test material as well as the reactive surface area. This study demonstrates that the textural and microstructural properties of the parent material have a significant influence on the chemical composition of the product phase. Moreover, our data highlight the importance of effective fluid-mediated element exchange between the fluid at the reaction interface and the bulk solution controlled by the local microstructure.

1. Introduction

Carbonates are of key importance in the lithosphere, the hydrosphere and the biosphere of planet Earth. They are directly involved in the terrestrial C, Ca, and Mg cycles and are important elements in the metabolism of most organisms (Tipper et al., 2006; Black et al., 2006; Fantle and Tipper, 2014). Moreover, carbonates are amongst the most important archives of planet Earth, recording proxy data on climate dynamics and biosphere evolution as far back as the Precambrian (Awramik, 1971; Kaufman et al., 1991; Burns et al., 2009). From an applied perspective, carbonates host about 50 % of the known hydrocarbon reserves (e.g., Warren, 2000).

All carbonates, however, are subject to post-depositional/post-secretion alteration during diagenesis and may undergo one or more cycles of transformation from metastable to stable phases (Friedman, 1964; Folk, 1965; Lippman and Bathurst, 1993; Morse et al., 2007; Hood van Smeerdijk et al., 2012; Geske et al., 2012, Gregg et al., 2015, Swart, 2015). The thermodynamic stability and composition of the mineral phases is linked to external variables such as temperature, pressure, and the matrix composition (fluid or solid) from which the mineral is formed. Changes in external conditions, such as pressure, temperature or fluid composition, lead

to compositional adjustments of the mineral phases, which might or might not be completed depending on the kinetics of the reaction. Variations in the chemical composition of carbonate minerals, for example, either in the form of reaction rims or gradual chemical zoning, are direct records of this process. Therefore, disequilibrium textures can be used to reconstruct the temporal evolution of mineral reactions in natural geological environments, if the relevant kinetic parameters are known (e.g., Müller et al., 2008; 2012; Helpa et al. 2014). Aragonite, i.e., orthorhombic $CaCO_3$, is metastable in most marine and terrestrial depositional environments and is commonly transformed to low-Mg calcite or various magnesian carbonates during early to late burial diagenesis (Morse et al., 2007).

The process of dolomitization, i.e., the replacement of calcium carbonate ($CaCO_3$) by dolomite [$CaMg(CO_3)_2$], has been a major focus of carbonate research given its great academic and industrial significance (Warren, 2000). Dolomite precipitation and replacement reactions have been the subject of numerous experimental and field studies, including microbially-induced precipitation under ambient conditions (Vasconcelos et al., 1995; Warthmann et al., 2000; Pacton et al., 2010; Geske et al., 2015b) and inorganic reactions at elevated temperatures and in a variety of fluid chemistries (e.g., Graf and Goldsmith, 1956; Katz and Matthews, 1977; Sibley, 1990; Miura and Kawabe, 2000; Roberts et al., 2013).

Test material for hydrothermal alteration experiments included abiogenic carbonates and powdered samples of fossil and recent biogenic Ca-carbonates (e.g., Land, 1967; Grover and Kubanek, 1983; Bullen and Sibley, 1984). Most studies, however, focused on the stability relationships in carbonate-fluid systems (e.g., Graf and Goldsmith, 1955; Rosenberg and Holland, 1964; Johannes, 1966; 1968; 1969; Rosenberg et al., 1967), on the influence of fluid composition on the chemical composition and mineralogy of the reaction product (e.g., Grover and Kubanek, 1983; Sibley, 1990), and the stoichiometry of the product dolomite (e.g., Kaczmarek and Sibley, 2007; 2011; 2014). The Ca:Mg ratio of the fluid has proven to be an important factor controlling the rate of dolomitization (e.g., Sibley, 1990; Sibley et al. 1994; Kaczmarek and Sibley, 2007; 2011).

So far, only a few studies included any description and analysis of the microstructure of the replacement products (e.g., Land, 1967; Grover and Kubanek, 1983; Bullen and Sibley, 1984; Kaczmarek and Sibley, 2007; Perdikouri et al., 2008; 2011; Jonas et al., 2015). Nonetheless, the microstructure of the parent carbonate material, in particular its permeability and reactive surface area, as well as their evolution through diagenetic (replacement) processes, are critical for the

quantification of both rates and spatial patterns of the dolomitization of carbonates in natural environments, e.g., through reactive transport modeling (Jones and Xiao, 2005; Whitaker and Xiao, 2010; Al-Helal et al., 2012).

A study of the replacement of single crystals of calcite by Mg-carbonates (Jonas et al., 2015), documented that spatial variations of the chemical composition of reaction products within the reaction rim can be related to local gradients in the composition of the pore fluid within the evolving reaction rim. Specifically, the limited transport of Ca and Mg through the pores of the reaction rim results in the development of compositional gradients within the fluid across the rim. The development of such gradients, however, is controlled by several factors such as the porosity, the permeability, the reactive surface area, and the water-to-mineral ratio.

This study focuses on the reaction of biogenic and abiogenic aragonite test materials with a 0.9 M $MgCl_2$ aqueous solution at 200 °C. The experimental conditions, i.e., the presence of highly concentrated saline solutions and a high reaction temperature, were chosen to i) focus on hydrothermal carbonate replacement reactions occurring in the burial environment and ii) to allow for sufficient reaction to occur on a laboratory timescale. Characterization of transport properties allows for quantitative assessment of the effects related to the initial compositional difference between the fluid and the carbonate solid, results of which can then be extrapolated to more natural fluid compositions and longer timescales.

To evaluate the effect of sample geometry on the replacement reaction, we have chosen three different aragonite test materials to represent variable reactive surface areas and fluid pathways. Specimen of abiogenic single crystals of aragonite, portions of the biogenic skeleton of the coral Porites sp. and the shell of the bivalve Arctica islandica were used as test materials. Comparison of rates and processes in aragonites with different textural and microstructural properties is a novel approach and allows for a quantitative assessment of the relative importance of transport and interface-limited alteration reactions. The combination of different analytical methods such as scanning electron microscopy, electron backscatter diffraction, and X-ray micro-computed tomography reveals new and detailed information about the microstructural evolution taking place during the replacement reactions.

The aims of this paper are threefold: (i) results of alteration experiments on three aragonite test materials with identical chemical composition but different textural properties are documented and interpreted in a process-related context; (ii) variations in the chemical composition of the newly formed reaction fronts are analyzed at high spatial resolution to assess

the chemical gradients within the pore fluid of each test material; (iii) the analysis of the replacement process as a function of time up to complete transformation performed for Porites sp. samples. This was done with regard to the evolution of the chemical composition and the transient microtextures of the product reaction front.

2. Materials and methods

2.1 Aragonite test material

To evaluate the effect of sample geometry and initial microstructure of the parent material on the replacement process, different aragonitic materials were used for the hydrothermal experiments. Fragments of natural single crystals of aragonite represent the compact, abiogenic end-member setting with a very low initial porosity providing a very small initial surface area for mineral-fluid interaction. Fragments of the shell of the bivalve Arctica islandica were taken as an intermediate setting, representing a complex organo-mineralic composite material with individual aragonite platelets and fibers surrounded by thin layers of organic materials (Schöne, 2013; Immenhauser et al., 2016). Finally, fragments of the skeleton of the coral Porites sp. represent the porous end-member of the text materials used here. The highly porous coral skeleton (Cuif and Dauphin, 2005) allows fast fluid access within the test material and exposes a very large reactive surface area. The use of aragonite materials with different sample geometry and microstructure as described above allows the identification of the relevant parameters that control the mechanism and overall rate of the replacement process. The structural characteristics and representative chemical compositions of the different aragonite fragments are listed in **Tabs. 1&2**.

2.1.1 Single crystals

Natural single crystals of aragonite (Böhmen, Germany) were prepared by cutting fragments perpendicular to the (001) surface from larger, columnar crystals with a pseudohexagonal outline using a diamond saw. The size of the single crystal fragments was ~ 4 × 4 × 4 [mm]. The initial weight of the fragments was ~ 224 – 225 mg (**Tab. 1**).

2.1.2 Arctica islandica

Cube-shaped subsamples of ~ 4 × 4 × 4 [mm] were cut from the aragonitic shells of recent samples of the bivalve A. islandica using a diamond saw. Shells were dredged off Iceland in 2013 in water depths of about 80 m and represent adult specimen of, on average, 15 years of age as based on counting of growth increments (Immenhauser et al., 2016). The initial weight of the shell subsamples varied between 131 mg – 140 mg (**Tab. 1**).

2.1.3 Porites sp.

Cube-shaped subsamples of ~ 4 × 4 × 4 [mm] were cut with a diamond saw from a recent coral specimen sampled on a research cruise in the Maldives outside of protected areas in 2012. The initial weight of the coral subsamples varied between 109 mg – 149 mg (**Tab. 1**).

2.2 Experimental setup

A solution containing 0.9 M $MgCl_2$ and 0.015 M $SrCl_2$ was prepared using anhydrous $MgCl_2$ (Sigma-Aldrich Chemie GmbH, ≥ 98 %), $SrCl_2 \cdot 6H_2O$ (Merck, 99 %) and distilled water. In each experiment, a Teflon©-lined steel autoclave was filled with one fragment of aragonite and 0.9 - 1.0 mL of liquid (**Tab. 1**). The autoclaves were placed in a furnace held at 200 °C for different reaction times between one and 20 days (**Tab. 1**). The time-series experiments were conducted by running five parallel experiments of different run durations rather than sampling the fluid of a single experiment at different times in order to keep the water to rock ratio (W/R) constant. The pressure was not controlled independently, but the reaction temperature of 200 °C corresponds to a saturated vapor pressure of approximately 16 bars. After various reaction times, the autoclaves were removed from the furnace and left to cool down to room temperature under ambient conditions for ~ 60 minutes. Both the reacted aragonite samples and the fluid were subsequently removed from the autoclaves for analysis. The reacted samples were then washed with distilled water to remove any remaining solution from the surface and dried in a drying cabinet at 100 °C overnight. One reacted sample from each experiment was embedded in epoxy resin and polished to half of its size. The microstructures and chemical composition of the

resulting cross-sections were then analyzed by scanning electron microscopy and electron microprobe analysis (see below).

2.3 Analytical methods

2.3.1 Scanning electron microscopy (SEM)

The microstructure of the polished cross sections and the surface of the reacted fragments were studied using a JEOL 840 SEM at the Westfälische Wilhelms-University (WWU) in Münster, Germany, and a Zeiss-LEO 1530, high resolution thermally-aided field-emission scanning electron microscope at the Ruhr-University in Bochum (RUB), Germany. The working distance was 12 mm for analysis of the crystal surfaces and 19 mm for analysis of the polished cross sections. The accelerating voltage was 20 kV.

2.3.2 Electron microprobe analyzer (EMPA)

The spatially-resolved chemical composition of the reacted fragments was measured using a Cameca SX50 and a Cameca SXFiveFE electron microprobe at RUB. Measurements were performed at an accelerating voltage of 15 kV and a probe current of 10 nA with a 8 µm defocussed beam. The counting time was 40 s on peak and 40 s on background, respectively. Ca, Mg, Fe and Mn were measured using K_α-lines and Sr was measured using the L_α-line. Pyrope [$Mg_3Al_2(SiO_4)_3$] was used as a reference material for Mg, spessartine [$Mn_3Al_2(SiO_4)_3$] for Mn, wesselsite ($SrCuSi_4O_{10}$) for Sr and andradite [$Ca_3Fe_2(SiO_4)_3$] for Ca and Fe for measurements with the SX50. For measurements using the SXFiveFE, MgO was used as a reference material for Mg, rhodonite ($MnSiO_3$) for Mn, $SrSO_4$ for Sr, diopside ($CaMgSi_2O_6$) for Ca and almandine [$Fe_3Al_2(SiO_4)_3$] for Fe. Representative microprobe analyses are shown in **Tab. 2**.

2.3.3 X-ray computed micro-tomography (µ-CT)

The three-dimensional geometry of the reaction front and the newly developed microstructures were investigated by X-ray micro-computed tomography (µ-CT) analysis performed using a SKYSCAN 1173 scanner at the University of Lausanne, Switzerland. The

non-destructive measurements of whole reacted fragments were conducted with 360° rotation and a step size of 0.2°. Eight frames were measured for 1250 ms at every step. The total scan time for each sample was about 5 h. All scans were performed with an Al-filter, at an accelerating voltage of 60 kV and a beam current of 130 µA. The 3D-spatial resolution was 5 × 5 × 5 µm per voxel. The SKYSCAN software package was used for volume rendering, image reconstruction and visualization.

2.3.4 Inductively coupled plasma optical emission spectrometry (ICP-OES)

For analysis of the chemical composition of the reacted fluid, 0.1 mL of the fluid was first diluted with 1 mL of 3.0 M HNO_3 and 2 ml of deionized water (> 18.1 MΩ cm^{-1}). A Thermo Fisher Scientific iCAP 6500 DUO inductively coupled plasma optical emission spectrometer was used to measure the concentrations of Mg, Ca, Sr, Fe, Mn, and Ba. The BSC-CRM-512 and BSC-CRM-513 reference materials were analyzed with a 1σ-reproduciblity of 0.18 % and 0.36 % for Mg, 0.081 % and 0.002 % for Ca, 22 µg/g and 1 µg/g for Sr, 17 µg/g and 12 µg/gfor Fe and 1 µg/g and 1 µg/g for Mn, respectively. Based on 62 replicate analyses of the referencœ materials BSC 512 (Dolomite) and BSC 513 (Limestone), the relative deviation from the certified values varies between 1 to 8% for the main constituents Ca, Mg and Sr. A five point calibration curve (4 working standards + blank) was used to calculate the concentration of each element. The multi-element working standards were prepared to meet the requirements of carbonates, i.e. to match the matrix. All measured data points lie on the calibration curve. The lowest calibration point exceed the background reading by at least 50%.

3. Results

The reaction of the aragonite fragments with a Mg-rich fluid leads to the replacement of aragonite by a series of distinct Mg-carbonate phases with different Mg:Ca ratios. The small volume of reaction products produced in the course of the experiment as well as physical separation of the reaction rim from the aragonite host material did not allow X-ray diffraction (XRD) analyses, limiting detailed mineralogical information. Thus, we cannot determine whether Mg-Ca carbonates with near-stoichiometric dolomite compositions are dolomite or very high magnesium calcites (VHMC), i.e., a carbonate with a dolomite-like stoichiometry/composition,

but the crystallographic attributes of calcite. The latter has been shown to be an intermediate product that eventually recrystallized to dolomite during the replacement process (see review of Gregg et al., 2015). Information on the lattice structure would provide valuable information on the exact reaction path, but we emphasize that the focus of the present study is on the formation of carbonate phases with distinct chemical compositions as controlled by transport properties and the resulting local fluid chemistry.

In all cases, the reaction involves the formation of a porous, polycrystalline reaction rim built of small Mg-carbonate rhombs that progressively replace the biogenic and abiogenic aragonite precursors (**Fig. 1**). A sharp reaction interface separates the reaction front from the unreacted parts of the samples. Both shape and size of the original aragonite samples are preserved throughout the reaction. We do, however, also recognize significant differences between the different test materials with regard to the microstructure, the number and chemical composition of the newly formed Mg-carbonate phases, and the rates of reaction.

3.1 Aragonite single crystals

The single crystals are replaced along a reaction rim that consists of four different Mg-carbonate phases. The product Mg-carbonate phases form a layered texture as identified in the BSE images (**Fig. 1A**). Isolated "patches" of unreacted aragonite are preserved in the reaction front (**Fig. 1A**). The different product phases and the remaining aragonite patches are separated by a distinctive boundary.

The reaction front replacing the single crystals advances parallel to the former crystal surface towards the center. The reaction front also migrates from fissures that crosscut the crystal from different directions (**Fig. 2**). In the outermost part of the reaction rim (adjacent to the reservoir fluid), a zone of near-stoichiometric magnesite (X_{Mg} = 0.97) is present (zone 1). Towards the unreacted aragonite core, this outer zone is followed by two additional layers (zone 2, which is partly interspersed with zone 1, and zone 3) that are progressively enriched in Ca (X_{Mg} = 0.79 for zone 2 and X_{Mg} = 0.34 for zone 3, respectively). The layered structure formed by zone 3 is significantly broader than the ones formed by zones 1 and 2. Finally, a fourth zone is present near the interface separating the reaction rim from the unreacted core of the aragonite crystal. Zone 4 is built of elongated sub-units oriented perpendicular to the reaction rim and the crystal

surface. This product phase yields the lowest Mg-concentration with an X_{Mg} = 0.07. A slight increase in Sr of up to X_{Sr} = 0.001 – 0.006 can be observed for zones 3 and 4 (**Tab. 2**).

Scanning electron microscopy analysis reveals that the outermost part of the reaction rim is built of rhombohedral crystals (**Fig. 3A**). Some of the larger, newly formed crystals have "flat" corners that form additional pentagonal planes. Micropores can be observed in zone 1 and in the innermost part of zone 3 (**Fig. 1A**). Large, partly connected cavities or "macropores" (~ 40 – 150 µm in length and ~ 10 – 60 µm in width) elongated parallel to the reaction rim are observed between zones 3 and 4 and the unreacted aragonite core (**Fig. 4A**). In some portions of the reaction rim, small single cavities or gaps (~ 30 – 180 µm in length and ~ 5 – 30 µm in width) can be observed between zones 1 and 2.

3.2 Arctica islandica bivalve shell

Samples of Arctica islandica are experimentally replaced by a reaction rim divided into three compositionally distinct sub-zones (**Fig. 1B**). In the outermost part of the reaction front, adjacent to the reservoir fluid, magnesite (zone 1) forms with a mole fraction of X_{Mg} = 0.90. The magnesite zone is followed by two zones of Mg-Ca carbonate: an intermediate zone (2) with X_{Mg} = 0.46 and an innermost zone (3) with a lower X_{Mg} = 0.38 at the interface to the unreacted aragonite core. An increase in Sr from X_{Sr} = 0.002 in zone 1 to X_{Sr} = 0.02 – 0.25 in the Ca-rich portions of the reaction rim can be observed, albeit with a pronounced spatial variability. However, this trend cannot be observed in every area of the sample (**Tab. 2**).

X-ray computed microtomography analysis revealed that the thickness of the reaction rim varies significantly within one fragment, depending on the orientation and position of the cross section. Scanning electron microscopy analysis of cross sections perpendicular and parallel to the outer shell surface do not reveal any significant differences in the chemical composition or microstructure of the reaction front.

Scanning electron microscopy analysis indicates that rhombohedral crystal forms are dominant for the newly precipitated carbonates that build the polycrystalline reaction rim, but some of the crystals exhibit pentagonal surfaces (**Fig. 3B**). Comparably large secondary pore space (~ 3 – 25 µm in diameter) is formed in zones 1 and 2, whereas zone 3 displays a more compact microstructure with overall smaller secondary pores not exceeding 2 µm in diameter

317 (**Fig. 1B**). An irregular gap separates the reaction front from the unreacted aragonite core (**Fig.**
318 **4B**). Zone 3 and some portions of zone 2 are partly disrupted by irregular cavities.
319

3.3 Porites sp. coral skeleton

Three compositionally distinct Mg-carbonate product phases replace the Porites sp. coral skeleton samples at different reaction stages. The experimental time-series using the Porites sp. samples allows for an assessment of the change in product phases as a function of time until complete transformation. After 24 h of reaction (**Fig. 5B**), a thin zone (average thickness ~ 35 µm) of porous magnesite formed along the outer margins of the coral skeleton, i.e., along the structures close to the original surface. This magnesite zone (1) is characterized by a distinctive Mg-concentration gradient. The mole fraction of Mg in zone 1 decreases from the outer part of the rim adjacent to the surface of the fragment (X_{Mg} = 0.93) towards the reaction interface (X_{Mg} = 0.81). After 48 h of reaction (**Fig. 5C**), a second zone (2) with a lower mole fraction of Mg (X_{Mg} = 0.41) formed between zone 1 and the unreacted aragonite. In the central portions of the sample, zone 1 is significantly thinner (average thickness ~ 10 µm). After five days (**Fig. 5D**), a very thin layer of Mg-Ca carbonate (zone 3) formed an overgrowth on top of zone 1 in the central portions of the coral sample. The Mg-Ca carbonate that makes up zone 3 has a higher mole fraction of Mg than that of zone 2 (X_{Mg} = 0.45). After ten days (**Fig. 6E**), very few isolated remnants of the former aragonite skeleton remain and magnesite (former zone 1) has been almost completely replaced by Mg-Ca carbonate (former zone 3). Small remnants of magnesite, however, are present at the corners of the sample. Finally, after 20 reaction days, the aragonitic coral skeleton is completely replaced by Mg-Ca carbonate (**Figs. 1C & 5F**). The mole fraction of Sr decreases from X_{Sr} = 0.01 in the unreacted material to X_{Sr} = 0.001 – 0.003 in all product phases (**Tab. 2**).

Scanning electron microscopy analysis documents that the highly porous reaction rim is built of well-defined rhombohedra (**Fig. 3C**). The replacement reaction is accompanied by the formation of an elongated gap along the interface between the reaction rim and the aragonite core. This gap results in the development of irregularly distributed pore space in the center of the single skeletal elements of the former aragonite sample after complete transformation to Mg-calcite (**Figs. 1C & 5C**). Petrographically speaking, the bulk of the coral skeleton ultra-structure is completely replaced during the early stages of the reaction. Conversely, some of the thick-walled structural elements still contain unreacted aragonite after five reaction days (**Fig. 7**).

3.4 Fluid composition

The compositional evolution of the fluid (**Fig. 8**) was monitored with time. The experiments used coral skeleton samples and corresponding fluids, since Porites sp. was the aragonitic test material that displayed the highest reaction progress after 20 days of reaction. Results indicate that the total concentration of Mg in the fluid reservoir decreases within the first ten days of reaction from the initial 0.9 mol/kg to ~ 0.30 mol/kg, followed by a slight increase up to 0.35 mol/kg after 20 days. The Ca- and Sr- concentrations continuously and concomitantly increase from 0.0 mol/kg and 0.015 mol/kg in the starting solution to ~ 0.53 mol/kg and ~ 0.02 mol/kg, respectively (**Tab. 3**). The Ca:Mg ratio in the reservoir fluid thus increases from 0.75 to 2.73 from day one to day ten of the reaction, followed by a decrease to 2.41 after 20 days.

3.5 Reaction progress

The time-dependent experiments with the Porites sp. fragments demonstrate that the number and arrangement of the different zones is transient. Throughout the experiments, both the reaction rim and the gap at the reaction interface progress simultaneously towards the center of the fragment. Finally, the gap along the reaction interface converges to form a central cavity within the former aragonite sample after complete transformation. Two sets of observations allowed us to quantify the reaction progress of Porites sp. as a function of time: (i) Coral fragments were the test material with the highest reaction progress after 20 reaction days based on weight loss and inspection of SEM images; (ii) the reaction rim replacing the aragonitic coral is chemically more homogeneous relative to those found in the other test materials.

All reacted samples show a decrease in weight after completion of the experiments (1.1 – 1.8 wt.% for the single crystals, 3.3 – 4.7 wt.% for A. islandica and 0.5 – 8.0 wt.% for Porites sp.). The difference in the molecular weight of the Mg substituting for Ca in the product carbonate phases causes a decrease in weight that is proportional to the amount of aragonite transformed, i.e., to the amount of Ca substituted by Mg, although there might be some additional contribution of the net solution of Ca-carbonate and organics to the total weight loss. The single crystals, for example, have a relatively thin reaction rim and show the smallest change in weight. After 20 days of reaction, fragments of Porites sp. are almost completely transformed. Accordingly, they show the largest decrease in weight.

4. Interpretation and discussion

4.1 Basic considerations on the replacement of aragonite by Mg-rich carbonate phases

Three types of experimental aragonite materials with different fabrics and micro-textures were investigated to evaluate the effect of fluid pathways and reactive surface areas during hydrothermal replacement by Mg-carbonates. Generally, the number of chemically distinct secondary carbonate phases decreases with increasing porosity and reactive surface area of the test material. Single crystal aragonite samples develop up to four different zones within the reaction rim, each characterized by a specific Mg- and Ca-content. Conversely, alteration in the highly porous Porites sp. samples results in a comparably simple setting with a thin magnesite fringe at the fluid-carbonate interface overlying what is otherwise a Mg-Ca-carbonate with a very narrow compositional range. The replacement reaction can be described in a generalized and simplified form by taking the element exchange between the fluid phase and a solid-solution Mg-carbonate into consideration:

$$CaCO_3\,(s) + x\,Mg^{2+}\,(aq) \rightarrow Ca_{1-x}Mg_xCO_3\,(s) + x\,Ca^{2+}\,(aq)\ (\textbf{Eqn. 1})$$

We note that the overall replacement of Ca by Mg in the carbonate lattice of the secondary phase results in a decrease in the molar volume. For illustration, one can use the molar volume of magnesite and stoichiometric dolomite to calculate the maximum negative molar volume change. It ranges from -17.92 % (-6.12 cm^3/mol) for aragonite-magnesite replacement to -5.80 % (-3.96 cm^3/mol) for aragonite-dolomite replacement.

4.1.1 Evolution of the reservoir fluid composition

The evolution of the chemical composition of the reservoir fluid is documented for the time series with samples of Porites sp. The replacement of aragonite by Mg-carbonate is accompanied by the incorporation of Mg^{2+} into the secondary carbonate phase and the simultaneous release of Ca^{2+} into the fluid phase according to eq. 1. In the case of Porites sp., this leads to a continuous increase of the Ca:Mg ratio in the reservoir fluid within the first ten days of reaction (**Fig. 8**). After 20 days, we observe a decrease in the fluid Ca:Mg ratio due to an increase in the fluid Mg-concentration. The increase in the fluid Mg concentration in the final stages of the

reaction is potentially caused by the secondary replacement of magnesite by a Mg-Ca carbonate and the dissolution of remnants of magnesite at the fringes of the cube-shaped sample. Since unreacted samples of Porites sp. contained a mole fraction of X_{Sr} = 0.01, both Ca and Sr are released into fluid through the dissolution of the parent aragonite material. This results in a parallel trend for both concentrations as a function of time (**Fig. 8A**).

4.1.2 Behavior of strontium during the replacement process

All of the different aragonitic test materials used for the experiments contain significant amounts of Sr that is known to substitute into Ca-sites within the carbonate lattice. The rather large Sr-cation is less compatible in the crystal structure of the product Mg-carbonate phases than in the parental aragonite. This is mainly due to the smaller difference in the ionic radii between Ca^{2+} (1.06 Å) and Sr^{2+} (1.27 Å) compared to Mg^{2+} (0.78 Å) and Sr^{2+}. Thus, according to Goldschmidt's rule, the substitution of Ca^{2+} for Sr^{2+} should be favored over the substitution of Mg^{2+} (Morse and Mackenzie, 1990), and the incorporation of Sr^{2+} into the reaction rim will occur more frequently if Ca-rich product phases precipitate. In other words, dissolution of Sr-bearing aragonite will progressively enrich the fluid in Sr when it is not re-incorporated into the product magnesite or Mg-Ca-carbonate. This is in agreement with the observed Sr-content in the Ca-rich reaction products of the single crystals and the samples of the bivalve A. islandica. This trend illustrates that trace element behavior during alteration reactions is controlled by the major element composition of the product phases. We note, however, that Sr substitution into the calcite lattice may be enhanced in response to the deformation of the lattice induced by the presence of magnesium, as suggested by Mucci and Morse (1984). Here, the presence of Mg "widens" the neighboring Ca-sites, promoting the incorporation of the larger Sr cation by substitution. Similarly, Mueller et al. (2012) showed a strong compositional dependence of the activation energies for solid-state diffusion of divalent cations in dolomite. They attributed this to the distortion of the layered dolomite lattice by the diffusive substitution process that eventually approaches the structure of the simple calcite lattice and its corresponding activation energies.

4.2 Reaction mechanism and rate of the replacement reaction

4.2.1 Reaction mechanism of aragonite to Mg-carbonate replacement

448 Scanning electron microscopy images of the surface of the reaction rim show that the
449 newly formed carbonate phases consist of small Mg-carbonate rhombohedra, which were not
450 present in the precursor aragonite (**Figs. 3A,B**). The observation that aragonite is replaced by a
451 polycrystalline reaction front of newly precipitated carbonate rhombs and the fact that the
452 different phases are separated by a sharp interface (**Figs. 1,2,4,5**) suggest that aragonite
453 replacement takes place by a dissolution-precipitation mechanism (c.f. Putnis, 2009 and
454 references therein). This interpretation is in agreement with previous work (Katz and Matthews,
455 1977; Grover and Kubanek, 1983; Sibley, 1990). Specifically, the presence of a reaction rim
456 consisting of small carbonate rhombohedra has been reported for both natural (Wenk and Zenger,
457 1983; Pearce et al., 2013) and experimental (Land, 1967; Grover and Kubanek, 1983; Sibley,
458 1990; Zempolich and Baker, 1993; Kaczmarek and Sibley, 2007; Perdikouri et al., 2008; 2011)
459 carbonate replacement reactions. The bulk morphology of the aragonite sample remains largely
460 unchanged despite significant alteration. This tentatively implies a pseudomorphic replacement of
461 primary aragonite by secondary Mg-carbonate phases. This notion is in agreement with previous
462 experimental studies on carbonate-carbonate replacement reactions that take place by a
463 dissolution-precipitation mechanism (Blake et al., 1982; Grover and Kubanek, 1983; Bullen and
464 Sibley, 1984; Zempolich and Baker, 1993; Perdikouri et al., 2008; 2011; Jonas et al., 2015).
465
466 **4.2.2. Significance of intra- and inter-crystalline organic matrix**
467 Despite the fact that all experimental materials used in this study are composed of
468 aragonite, they differ in important aspects. This includes the fact that the coral skeleton and the
469 bivalve shell are built of inorganic/organic composite units whereas the aragonite single crystal is
470 purely inorganic in nature. Thus, one of the relevant questions in the context of this study is if the
471 presence of an organic matrix affects the replacement kinetics of biogenic test materials.
472 Compositionally, the aragonitic bivalve shell contains 95–99% calcium carbonate. The remaining
473 material consists of proteins, polysaccharides and proteoglycans. These are generally described as
474 'organic matrix' (Marin & Luquet, 2004; Karney et al., 2011). Coral skeletons are composite
475 acellular structures, in which organic macromolecules (mainly protein, lipids and sugars) are
476 intimately associated with mineral phases (Farre et al., 2010; Cuif et al., 2011). The concept of an
477 intra- and inter-crystalline organic fraction in biominerals has been described by early workers
478 (Towe and Thompson, 1972; Sykes et al., 1996) and is now the topic of intense research (see

discussion in Cuif et al., 2011). It is conceivable that organic matter covering biominerals in the primary shell retards the effects of diagenetic fluids.

Ongoing work by some of the authors documents that the organic matrix within A. islandica shells reacts to hydrothermal alteration experiments at temperatures of 100 to 175 °C, irrespective of the composition of the reactive fluid. At 100 °C, the aragonitic biomineral fabric of the bivalve remains essentially unaltered but a partial redistribution and darkening of intra-shell organic matter is observed. Evidence for organic matter redistribution comes from fluorescence microscopy. At 175 °C, the organic matter is dissolved and small depressions mark the former position of organic material. These observations are in good agreement with the fact that organic matter starts to decompose at ~160 °C (Martell et al., 1975; Motekaitis et al., 1982; Boles et al., 1987; Crossey, 1991; Benezeth et al., 1997). Given that the experiments performed in this study included fluid temperatures of 200 °C, we postulate that most, if not all, of the extra-crystalline organic matrix within the biogenic test organisms was decomposed within a few hours after the start of the alteration experiment.

This does not necessarily imply that the presence of a former organic phase has no impact on processes and reaction rates during these experiments and the issue of intra-crystalline organic matter is complex. One critical aspect is the interaction of organic compounds such as polysaccharides and Mg aquo-complexes in the aqueous fluid (Zhang et al., 2012). Specifically, the chemical bonding between the Mg^{2+} ions, that is also a major controlling factor in Mg isotope fractionation between fluid and solid (Mavromatis et al., 2013, Schott et al., 2016), and one to several ordered layers of water molecules may be important with respect to the Mg^{2+} incorporation kinetics. In contrast to studies carried out at low temperatures, however, kinetic factors related to the dehydration of Mg aquo-complexes are less significant at elevated temperatures such as those investigated in this study (Pearce et al., 2012; Geske et al., 2015a). Nevertheless, the decomposition of organic matter might increase the porosity and permeability of test materials and results in a larger reactive surface. This notion is important and must be considered when comparing the replacement kinetics of inorganic and biogenic carbonates.

4.2.3 Spatial and temporal evolution of the pore fluid composition and its control on the precipitating phase and reaction rate

Whereas dissolution-precipitation is unarguably the operating replacement reaction mechanism, it is important to bear in mind that the replacement reaction is made up by a series of processes (i.e., dissolution of solids, transport of aqueous species within the pore fluid, precipitation of secondary phases) where individual rates can change in time and space during the overall replacement reaction (e.g., Mueller et al. 2010). Except for nucleation, all other processes proceed in a serial sequence and the slowest of these, i.e., the rate-limiting step, will determine the overall rate of reaction. Element transport (here dominated by diffusion) and interface-controlled dissolution-precipitation processes may exert a combined control on the reaction rate (e.g., Lasaga 1986). If the reaction rate is solely controlled by interface-controlled processes, i.e., either precipitation of the Mg-Ca carbonate or dissolution of the aragonite reactant, the fluid composition is likely to be effectively homogenous throughout the reaction system (e.g., see also Dohmen and Chakraborty, 2003). Previous studies indicate that the chemical composition of the replacement product is determined by the (local) composition of the reacting fluid (e.g., Rosenberg and Holland, 1964; Land, 1967; Rosenberg et al., 1967; Sibley, 1990; Tribble et al., 1995; Kaczmarek and Sibley, 2007; 2011, 2014; Jonas et al., 2015). Thus, spatial variations in the chemical composition of the solid product provides clues on local fluid composition and thus on the temporal evolution of concentration gradients that develop in the pore fluid of the reaction rim.

In experimental samples studied here, the amount of Mg in the newly precipitated Mg-Ca-carbonate product phase decreases with increasing distance from the outer surface of the product and the experimental reservoir fluid. For example, the outermost zone that consists of Ca-poor magnesite in all experimental samples has the highest Mg-content of all product phases. The formation of a reaction rim consisting of chemically distinct product phases is related to the transport of the relevant aqueous species that flow through the porous channels created by the negative molar volume change of the replacement reaction. As the width of the reaction rim increases during the reaction, the transport distance between the bulk solution and the reaction interface increases. Accordingly, the elemental exchange becomes less efficient. In case of sluggish diffusion, this leads to a compositional gradient in the pore fluid with respect to Mg and Ca and to the precipitation of a reaction rim with an evolving Mg and Ca content, as previously

described by Jonas et al. (2015). It is important to bear in mind that the local fluid composition controls the chemistry of the precipitating phase leading to a reaction rim that consists of different Mg-carbonate phases. Hence, the observed spatial compositional variations record the temporal evolution of the Ca:Mg ratio in the pore fluid at the reaction interface. This, in turn, suggests that the composition of the distant reservoir fluid is of secondary importance for the chemical composition of the product phases precipitating at the tip of the progressive reaction front, except for the earliest stages of the replacement process. At first sight, these implications seem to be in direct contradiction with the experimental work by Kaczmarek and Sibley (2011), who found that the Mg:Ca ratio in the (reservoir) fluid controls both the rate of the replacement reaction and the composition of the product. However, differences in the experimental setup, in particular with regard to the initial reactants, need to be considered. Kaczmarek and Sibley (2011) used powdered calcite of a size fraction of 40 – 60 µm, while large aragonitic samples of 3 – 4 mm in size were used in this experimental study. First, the powdered material provides a larger reactive surface area for mineral fluid interaction compared to the aragonite reactants used in this study, accelerating the rate of the replacement reaction. Second, the smaller size of the calcite grains used by Kaczmarek and Sibley (2011) implies a smaller distance for element transport from the outer surface to the center of the solid reactants. Consequently, the effect of transport-limitation is less pronounced in the powder experiments, which do not account for any textural features and which may only develop minor compositional gradients in the pore fluid due to the experimental setup. In such cases, where element transport is not the rate-limiting process, the bulk fluid phase is likely almost homogeneous in composition and therefore controlled by the bulk fluid composition, in agreement with the findings of Kaczmarek and Sibley (2011).

This interpretation is in line with a recent conceptual model of Jonas et al. (2015) for the replacement of calcite single crystals by Mg-Ca carbonate and magnesite. In the above study, a sequence of Mg-rich zones was observed that share similarities with the replacement patterns of single crystals of aragonite documented in this study. Most importantly, following a transitional stage characterized by Mg-Ca carbonate, magnesite replaced Mg-Ca carbonate despite a continuous increase of the Mg:Ca ratio in the fluid reservoir (Jonas et al., 2015). A similar process can be observed for samples of Porites sp. described in this study. This emphasizes the importance of local fluid composition determined by element fluxes as opposed to the temporal evolution of the bulk reservoir fluid as a unique proxy to trace the reaction process.

570

571 **4.2.4 Relation between textural and microstructural properties of aragonite and effective**
572 **element fluxes**
573

574 The replacement rate of aragonite is controlled by the diffusive transport through both the
575 fluid network initially present through the microstructure of the parent material and the secondary
576 porosity formed during the replacement. Based on these two parameters, the effect of the initial
577 texture on the reaction product and rate is discussed. The formation of Mg-Ca carbonate phase
578 requires a net flux of Mg (J_{Mg}) in moles per unit time and unit area through this network to the
579 reaction interface. The formation rate of Mg-rich carbonate (magnesite, Mg-Ca carbonate) can be
580 mathematically expressed as
581

582 $$\frac{dn_{Mg-Cb}}{dt} = A_{Arg} \times \frac{1}{X_{Mg}} \times J_{Mg} \quad \textbf{(Eqn. 2)}$$

583

584 In this equation, the term on the left hand side describes the number of moles of
585 magnesium (dn_{Mg-Cb}) precipitating in the Mg-Ca carbonate solid solution phase ($Ca_{1-x}Mg_xCO_3$)
586 over a given time increment (dt). On the right hand side, this rate is expressed by multiplying
587 the reactive surface area of the aragonite fragment (A_{Arg}) by the inverse fraction of Mg (X_{Mg}),
588 and the diffusive flux of Mg (J_{Mg}) across the evolving reaction rim. Accordingly, the formation of
589 Mg-Ca carbonates thus requires a counter diffusion flux of Ca from the dissolving aragonite
590 interface towards the bulk fluid reservoir. For a porous aggregate where replacement does not
591 follow a continuous propagation of a single reaction front (**Fig. 1A-C**) and occurs at different
592 reaction sites, the total formation rate of Mg-rich carbonate is given by the sum of the formation
593 rate of the individual reaction sites.

594 The local element flux and the local reaction rates at the individual reaction sites are
595 variable since replacement occurs faster at the edges of the porous aggregate. In general, the
596 diffusive flux of a species i (in this case either Mg^{2+} or Ca^{2+}) within each reaction rim is
597 controlled by its diffusion coefficient D_i, its concentration gradient (∇C_i) perpendicular to the
598 reaction rim, the tortuosity (τ) and the porosity (ϕ) within the rim, according to:
599

600 $$J_i = \phi \times \tau \times D_i \times \nabla C_i \qquad \textbf{(Eqn. 3)}$$

601

602 A higher reaction rate can be caused by increasing one or more of the following four
603 parameters ϕ, τ, ∇C_i and A_{Arg}. The initial material properties of the parent samples govern the
604 efficiency of element transport to and from the reaction interface. Consequently, the geometry of
605 the solid reactants also controls the exchange of the relevant aqueous species between the fluid at
606 the reaction interface and the bulk reservoir fluid surrounding the aragonite sample. This effect is
607 especially pronounced in the partly transformed single crystals representing the end-member of a
608 dense, impermeable aragonite material. In the case of single crystals, exchange of Mg and Ca
609 between pore-fluid and crystal can only occur by transport through the porous channels formed
610 due to the negative volume change along the reaction front, except for a small number of cracks
611 or fissures that were present in the unreacted crystals (**Figs. 1A&2**). Here, the molar volume
612 reduction and the transformation from aragonite to magnesite or Mg-Ca carbonate results in
613 volume loss at the reaction front resulting in the formation of porosity in the form of gaps and
614 cavities along the reaction interface. The formation of porosity within the experimental reaction
615 front is a commonly observed feature for several replacement reactions with an overall negative
616 volume change that takes place by a dissolution-precipitation mechanism (e.g., Putnis, 2009). The
617 formation of gaps or cavities at the reaction interface has also been observed for other closed
618 system experimental replacement reactions in other mineral systems (Pöml et al., 2007; Geisler et
619 al., 2010; Dohmen et al., 2013, Jonas et al., 2015). Conversely, in open system subsurface
620 replacement settings, evidence for such reaction front porosity is less obvious. The newly formed
621 pore space represents pathways for fluid flow within the aragonite test material that allows for a
622 continuous element exchange between the fluid at the reaction interface and the bulk reservoir
623 fluid (Putnis et al., 2005; Perdikouri et al., 2011; Raufaste et al., 2011).

624 Samples of the bivalve *A. islandica* initially exhibit a heterogeneously distributed micro-
625 porosity due to the complex organic-inorganic compound structure of these biominerals (Karney
626 et al., 2011). Moreover, as observed microscopically, fissures formed during the reaction that
627 crosscut the biogenic test material properties in different directions. These fissures and micro-
628 pores, particularly where water-soluble intra-crystalline organic material has been dissolved
629 between aragonite platelets and fibers, serve as pathways for reactive fluid. Micro-porosity and
630 related permeability result in faster reaction rates relative to the tight fabric of the single crystals.

These pathways promote a more efficient element exchange between the bulk solution and the solution at the reaction interface.

Samples of the coral Porites sp. have an even higher initial porosity and thus represent the permeable end-member allowing a very efficient element flux between the reaction front and the bulk fluid. Efficient transport apparently prevents the development of large compositional gradients within the fluid phase. As a result, the individual zones within the reaction rim are wider and only three instead of four product phases were recognized. Consequently, the porosity and permeability and the concentration gradient within the fluid are inversely correlated. Compared to the reaction rims of the impermeable single crystals, the smaller aqueous concentration gradient within the interconnected pore network of the rim replacing Porites sp. leads to a more homogeneous solid reaction rim.

We note, however, that the overall reaction rate is still higher for the reactants that are more porous. The reason for the more efficient reaction in case of Porites sp. is related to the larger reactive surface area of aragonite (larger surface to fluid volume ratio – eq. 2) and partly related to the micro-porosity present within the aragonite (eq. 3), which increases the element flux to and away from the local reaction site. Moreover, biogenic carbonates are essentially less stable/more reactive than their abiogenic equivalents (Böttcher and Dietzel, 2010). .

5. Implications

Considering that aragonite and high-Mg calcite replacement reactions occur in various environments, the processes discussed above are of significance. Particularly, the dolomitization of limestone (and de-dolomitization of dolostones, Ayora et al., 1998) is an important research field of both academic and applied significance (Waneless, 1979; Budd, 1997; Warren, 2000; Vandeginste et al., 2013). Here, we document that the porosity and permeability of the parent host rock is of fundamental importance in determining both the rate of the overall dolomitization process and the chemical composition of the products. This becomes especially important when comparing sharp and gradual dolomitization fronts in core material and outcrops. Whereas sharp reaction fronts are commonly interpreted to develop by a surface-controlled replacement process, gradual compositional changes are often indicative of transport-controlled processes. In some cases, dolomitization of limestone rock bodies takes place across a cm-thin alteration front, in other cases over distances of up to several meters (Ferry et al., 2011; Vandeginste et al., 2013).

On the basis of our experimental results, we propose that diffusive transport across the polycrystalline reaction rim is the rate-limiting step of the replacement process. The degree of "transport-limitation" decreases with increasing permeability of the parent material, i.e., the availability of fluid pathways in the host rock on a large scale, and vice versa. A diffusion-limited dolomitization process could also have a significant imprint on the isotopic signature of the rocks, as documented for the Mg isotopes in a metasomatic reaction zone at an exhumed contact between rocks of subducted crust and serpentinite in the Syros mélange zone (Pogge Von Strandmann et al. 2015).

The characterization of transport processes in chemical micro-environments and their incorporation into field scale transport simulations is one of the frontier research questions in the field of reactive transport modeling (Steefel et al., 2005). The fact that the permeability of the initial carbonate reactant controls the degree of transport limitation in carbonate replacement processes on a microscopic scale is an important factor that is not yet considered in reactive transport models that simulate dolomitization processes in natural carbonate sediments.

Acknowledgements

The authors would like to thank R. Neuser and C. V. Putnis for help with scanning electron microscopy, W. Köhler and Nils Jöns for help with electron microprobe analysis, and the Deutsche Forschungsgemeinschaft (DFG) for supporting this research through grant MU 2988/2-1 to Müller/Dohmen. Discussions within the framework of the DFG priority program CHARON are greatly acknowledged. Detailed and constructive reviews by S. Kaczmarek and two anonymous reviewers as well as editorial comments of Alfonso Mucci are greatly acknowledged and significantly improved the clarity of the paper.

Figure Captions

Fig. 1: Backscattered electron image of polished cross sections of reacted fragments of single crystals of aragonite (**A**), Arctica islandica (**B**) and Porites sp. (**C**). The reaction rims that form around the single crystal and shell fragments can be divided into different layers with different chemical composition and microstructure. The replacement of the fragments by Mg-

carbonates is also accompanied by the development of porosity, cavities and/or a trench within the reaction rim.

Fig. 2: Backscattered electron image of polished cross section of a partly transformed aragonite crystal. The arrows indicate the growth direction of the reaction front. The reaction rim spreads not only from the surface of the fragment, but also from a crack that penetrates the fragments perpendicular to the surface.

Fig. 3: Secondary electron image of the surfaces of reacted fragments of single crystals of aragonite (**A**), Arctica islandica (**B**) and Porites sp. (**C**). The reaction fronts that replace the aragonite fragments are built of small Mg-carbonate rhombs. The shape and size of the rhombs varies with the respective parent material.

Fig. 4: X-ray micro-tomography images of the reacted aragonite fragments (**A**: single crystal; **B**: Arctica islandica; **C**: Porites sp.). The µ-CT images show the development of a gap (dark) at the reaction interface of the single crystals and the samples of A. islandica (**A** and **B**) and the formation of large cavities adjacent to the reaction interface of the samples of A. islandica (**B**).

Fig. 5: Weight decrease of the aragonite single crystals, coral and shell fragments as a function of time. The largest decrease in weight can be observed for the coral fragments, whereas the change in weight of the single crystals is relatively small.

Fig. 6: Backscattered electron images of polished cross sections of an unreacted fragment of Porites sp. (**A**) and of reacted fragments after one, two, five, ten and 20 days of reaction (**B - F**). After one day, a thin layer of magnesite has formed as the only product phase close to the surface of the Porites sp. sample (**B**). After two days, a layer of dolomitic composition with X_{Mg} = 0.40 appears as a second product phase between the magnesite layer and the unreacted aragonite (**C**). After five days, an overgrowth of dolomitic composition starts to form on top of the magnesite layer (**D**), and after ten days, almost all of the magnesite has been replaced by a new layer of non-stoichiometric dolomite with X_{Mg} = 0.45 (**E**). After 20 days of reaction and complete transformation, non-stoichiometric dolomite with X_{Mg} = 0.45 is left as the only product phase (**F**).

Fig. 7: X-ray micro-tomography images of coral fragments that reacted for different times (**A**: one day; **B**: two days; **C**: five days; **D**: ten days). The µ-CT images show the development of the reaction front as a function of time. After one day, the fragment still consists of almost pure aragonite (in light gray color). The amount of unreacted material decreases as a function of time

until complete transformation to dolomitic composition of X_{Mg} = 0.45 after twenty days of reaction (see **Fig. 4.4C**).

Fig. 8: The concentrations of Ca and Sr (**A**) of the reacted fluid continuously increase as a function of time. The concentration of Mg (**A**) decreases from continuously within the first ten reaction days, followed by an increase in the final stages of the reaction, i.e., after 20 reaction days. The Ca/Mg ratio (**B**) in the bulk fluid increases within the first ten reaction days, followed by decrease in the final stages of the reaction.

References

Al-Helal, A. B., Whitaker, F., and Xiao, Y., (2012) Reactive transport modeling of brine reflux: dolomitzation, anhydrite precipitation, and porosity evolution. J. Sediment. Res. **82**, 196-215.

Ayora, C., Taberner, C., Saaltink, M. W. and Carrera, J. (1998) The genesis of dedolomites: a discussion based on reactive transport modeling. J. Hydrol. **209,** 346-365.

Awramik, S.M. (1971) Precambrian columnar stromatolite diversity: reflection of metazoan appearance. Science **174,** 825-827.

Benezeth P., Palmer D. A. and Wesolowski D. J., 1997, Dissociation quotients for citric acid in aqueous sodium chloride media to 150 °C. J. Solution Chem. **26**, 63–84.

Black, J. R., Yin, Q.-Z. and Casey, W. H. (2006) An experimental study of magnesium - isotope fractionation in chlorophyll - a photosynthesis. Geochim. Cosmochim. Acta, **70,** 4072-4079.

Blake, D. F., Peacor, D. R. and Wilkinson, B. H. (1982) The sequence and mechanism of low-temperature dolomite formation: calcian dolomites in a Pennsylvanian echinoderm. J. Sediment. Petrol. **52**, 59-70.

Boles, J.S., Ritchie, K., Crerar, D.A. (1987) Reducing the potential for migration of radioactive waste: Aqueous thermal degradation of the chelating agent disodium edta. Nuc. Chem. Waste Man. **7**, 89-93.

Böttcher, M. E. and Dietzel, M. (2010) Metal - ion partitioning during low - temperature precipitation and dissolution of anhydrous carbonates and sulphates. EMU Notes in Mineralogy, **10,** 139-187.

Budd, D. A. (1997) Cenozoic dolomites of carbonate islands: their attributes and origin. Earth-Sci. Rev. **42,** 1-47.

Bullen, S. B. and Sibley, D. F. (1984) Dolomite selectivity and mimic replacement. Geology **12**, 655-658.

Burns, B. P., Anitori, R., Butterworth, P., Henneberger, R., Goh, F., Allen, M. A., Ibanez-Peral, R., Bergquist, P. L., Walter, M. R. and Neilan, A. (2009) Modern analogues and the early history of microbial life. Precambrian Res. 1-38.

Crossey L. J., 1991, Thermal degradation of aqueous oxalate species. Geochim. Cosmochim. Acta **55**, 1515–1527.

Cuif, J.-P. and Dauphin, Y. (2005) The environmental recording unit in a coral skeletons: a synthesis of structural and chemical evidences for a biochemically driven, strepping-growth process in fibres. Biogeosciences 2, 61-73.

Cuif, J.-P., Dauphin, Y., Sorauf, J. E. (2011) Biominerals and Fossils Through Time. Cambridge University Press.

Dohmen, R. and Chakraborty, S. (2003) Mechanism and kinetics of element and isotopic exchange mediated by a fluid phase with implications for geothermometry, geospeedometry, and isotopic closure. Am. Mineral. **88**, 1251–1270.

Dohmen, L., Lenting, C., Fonseca, R. O. C., Nagel, T., Heuser, A. and Geisler, T. (2013) Pattern Formation in Silicate Glass Corrosion Zones. Int. J. Appl. Glass Sci. **4 (4)**, 357-370.

Fantle, M. S. and Tipper, E. T. (2014) Calcium isotopes in the global biogeochemical Ca cycle: Implications for development of a Ca isotope proxy. Earth – Sci. Rev. **129,** 148 – 177.

Farre, B., Cuif, J.-P. and Dauphin, Y. (2010) Occurrence and diversity of lipids in modern coral skeletons. Zoology **113**, 250-257.

Ferry, J. M., Passey, B. H., Vasconcelos, C. and Eiler, J. M. (2011) Formation of dolomite at 40-80 °C in the Latemar carbonate buildup, Dolomite, Italy, from clumped isotope thermometry. Geology **39**, 571-574.

Friedman, G.M. (1964) Early diagenesis and lithification in carbonate sediments. J. Sediment. Petrol. **34,** 777-813.

Folk, R. L. (1965) Some aspects of recrystallization in ancient limestones. In: Dolomitization and Limestone Diagenesis, SEPM Special Publication **13**, pp. 14-48.

Geske, A., Zorlu, J., Richter, D. K., Niedermayr, A. and Immenhauser, A. (2012) Impact of diagenesis and low grade metamorphosis on isotope ($\delta^{26}Mg$, $\delta^{13}C$, $\delta^{18}O$ and $^{87}Sr/^{86}Sr$) and

788 elemental (Ca, Mg, Mn, Fe and Sr) signatures of Triassic sabkha dolomites. Chem. Geol.
789 **332-333,** 45-64.
790 Geske, A., Goldstein, R. H., Richter, D. K., Buhl, D., Kluge, T., John, C. and Immenhauser, A.
791 (2015a) The magnesium isotope (δ^{26}Mg) signature of dolomites. Geochim. Cosmochim.
792 Acta **149,** 131-151.
793 Geske, A., Lockier, S., Dietzel, M., Richter, D. K., Buhl, D. and Immenhauser, A. (2015b)
794 Magnesium isotope composition of sabkha pore fluids and related (Sub-) Recent
795 stoichiometric dolomites, Abu Dhabi (UAE). Chem. Geol. **393-394,** 112-124.
796 Geisler, T., Janssen, A., Scheiter, D., Stephan, T., Berndt, J. and Putnis, A. (2010) Aqueous
797 corrosion of borosilicate glass under acidic conditions: A new corrosion mechanism: J.
798 Non-Cryst. Solids **356**, 1458-1465.
799 Graf, D. L. and Goldsmith, J. R. (1955) Dolomite-magnesian calcite relations at elevated
800 temperatures and CO_2 pressures. Geochim. Cosmochim. Acta **7**, 109-128.
801 Graf, D. L. and Goldsmith, J. R. (1956) Some hydrothermal syntheses of dolomite and
802 protodolomite. J. of Geol. **64**, 173-186.
803 Gregg, J. M., Bish, D., Kaczmarek, S. E. and Machel, H. (2015) Mineralogy, nucleation and
804 growth of dolomite in the laboratory and sedimentary environment: A review,
805 Sedimentology, **62**, 1749-1769.
806 Grover, J. and Kubanek, F. (1983) The formation of ordered dolomite from high-magnesium
807 calcite at 250°C to 350°C and 1500 bars: epitactic growth with optimal phase orientation,
808 and implications for carbonate diagenesis. Am. J. Sci. **283-A**, 514-539.
809 Helpa, V., Rybacki, E., Abart, R., Morales, L. F. G., Rhede, D., Jeřábek, P. and Dresen, G.
810 (2014) Reaction kinetics of dolomite rim growth. Contrib. Mineral. Petrol. **167**, 1001.
811 Hood van Smeerdijk, A. and Wallace, M. W. (2012) Synsedimentary diagenesis in a Cryogenicna
812 reef complex: Ubiquitous marine dolomite precipitation. Sediment. Geol., **255-256,** 56-71.
813 Immenhauser, A., Schoene, B., Hoffmann, R. and Niedermayr, A. (2016) Mollusc and
814 brachiopod skeletal hard parts: intricate archives of their marine environment.
815 Sedimentology **63**, 1-59.
816 Johannes, W. (1966) Experimentelle Magnesitbildung aus Dolomit + $MgCl_2$. Contrib. Mineral.
817 Petrol. **13**, 51-58.
818 Johannes, W. (1968) Experimentelle Sideritbildung aus Calcit + $FeCl_2$. Contrib. Mineral. Petrol.
819 **17**, 155-164.

820 Johannes, W. (1969) Siderit-Magnesit-Mischkristallbildung im System Mg^{2+}-Fe^{2+}-CO_3^{2-}-Cl_2^{2-}-
821 H_2O. Contrib. Mineral. Petrol. **21**, 311-318.
822 Jonas, L., Müller, T., Dohmen, R., Baumgartner, L., and Putlitz, B. (2015) Transport-controlled
823 hydrothermal replacement of calcite by Mg-carbonates. Geology **43**, 779-782.
824 Jones, G. D. and Xiao, Y. (2005) Dolomitization, anhydrite cementation, and porosity evolution
825 in a reflux system: Insights from reactive transport models. AAGP Bull. **89**, 577-601.
826 Kaczmarek, S. E. and Sibley, D. F. (2007) A comparison of nanometer-scale growth and
827 dissolution features on natural and synthetic crystals: Implications for the origin of
828 dolomite. J. Sediment. Res. **77**, 424-432.
829 Kaczmarek, S. E. and Sibley, D. F. (2011) On the evolution of dolomite stoichiometry and cation
830 order during high temperature synthesis experiments: An alternative model for the
831 geochemical evolution of natural dolomites. Sediment. Geol. **240 (1-2)**, 30-40.
832 Kaczmarek, S. E. and Sibley, D. F. (2014) Direct physical evidence of dolomite recrystallization.
833 Sedimentology **61**, 1862-1882.
834 Karney, G. B., Butler, P. G., Course, J. D., Richardson, C. A., Lau, K. H., Czernuszka, J. T. and
835 Grovenor, C.R.M. (2011) Identification of growth increments in the shell of the bivalve
836 mollusc Arctica islandica using backscattered electron imaging. J. Microsc. **241**, 29-36.
837 Katz, A. and Matthews, A. (1977) The dolomitization of $CaCO_3$: an experimental study at 252-
838 295°C. Geochim. Cosmochim. Acta **41**, 297-308.
839 Kaufman, A. J., Hayes, J. M., Knoll, A. H. and Germs, G. J. B. (1991) Isotopic compositions of
840 carbonates and organic carbon from upper Proterozoic successions in Namibia:
841 stratigraphic variation and the effects of diagenesis and metamorphism. Precambrian Res.
842 **49,** 301-327.
843 Land, L.S. (1967) Diagenesis of skeletal carbonates. J. Sediment. Petrol. **37**, 914-930.
844 Lasaga, A.C. (1986) Metamorphic reaction rate laws and development of isograds. Mineral. Mag.
845 **50**, 359-373.
846 Marin, F. and Luquet, G. (2004) Molluscan shell proteins. C.R. Palevol. **3**, 469-492.
847 Martell, A.E., Motekaitis, R.J., Fried, A.R., Wilson, J.S., MacMillan, D.T. (1975) Thermal
848 Decomposition of EDTA, NTA, and Nitrilotrimethylenephosphonic Acid in Aqueous
849 Solution. Can. J. Chem. **53**, 3471-3476.

Mavromatis, V., Gautier, Q., Bosc, O., and Schott, J. (2013). Kinetics of Mg partition and Mg stable isotope fractionation during its incorporation in calcite. Geochim. Cosmochim. Acta **114**, 188-203.

Miura, N. and Kawabe, I. (2000) Dolomitization of limestone with $MgCl_2$ solution at 150 °C: Preserved original signatures of rare earth elements as marine limestone. Geochim. J. **34**, 223-227.

Morse, J. W. and Mackenzie, F. T. (1990) Geochemistry of Sedimentary Carbonates. In Developments of Sedimentology **55** (eds. Morse, J. W. and Mackenzie, F. T.). Elsevier, Amsterdam, 707 pp.

Morse, J. W., Arvidson, R. S. and Lüttge, A. (2007) Calcium carbonate formation and dissolution. Chem. Rev. **107,** 342-381.

Motekaitis, R.J., Cox Iii, X.B., Taylor, P., Martell, A.E., Miles, B., Tvedt Jr, T.J. (1982) Thermal degradation of EDTA chelates in aqueous solution. Can. J. Chem. **60**, 1207-1213.

Mueller, T., Baumgartner, L. P., Foster, C. T. and Roselle, G. T. (2008) Forward modeling of the effects of mixed volatile reaction, volume diffusion, and formation of submicroscopic exsolution lamellae on calcite-dolomite thermometry. Am. Mineral. **93**, 1245-1259.

Mueller, T., Watson, E. B. and Harrison, T. M. (2010) Applications of diffusion data to high-temperature Earth systems, Rev. Mineral. Geochem. **72**, 997-1038.

Mueller, T., Cherniak, D. and Watson, E. B. (2012) Interdiffusion of divalent cations in carbonates: Experimental measurements and implications for timescales of equilibration and retention of compositional signatures. Geochim. Cosmochim. Acta **84**, 90-103.

Pacton, M., Gorin, G., Vasconcelos, C., Gautschi, H.-P. and Barbarand, J. (2010) Structural arrangement of sedimentary organic matter: Nanometer-scale spheroids as evidence of a microbial signature in early diagenetic processes. J. Sediment. . **80,** 919-932.

Pearce, M. A., Timms, N. E., Hough, R. M. and James, S. C. (2013) Reaction mechanism for the replacement of calcite by dolomite and siderite: implications for geochemistry, microstructure and porosity during hydrothermal mineralization. Contrib. Mineral. Petrol. **166**, 995-1009.

Pearce, C.R., Saldi, G.D., Schott, J., and Oelkers, E.H. (2012). Isotopic fractionation during congruent dissolution, precipitation and at equilibrium: Evidence from Mg isotopes. Geochim. Cosmochim. Acta **92**, 1-16.

881 Perdikouri, C., Kasioptas, A., Putnis, C. V. and Putnis, A. (2008) The effect of fluid composition
882 on the mechanism of the aragonite to calcite transition. Mineral. Mag. **72(1)**, 111-114.
883 Perdikouri, C., Kasioptas, A., Geisler, T., Schmidt, B. C. and Putnis, A. (2011) Experimental
884 study of the aragonite to calcite transition in aqueous solution. Geochim. Cosmochim.
885 Acta **75**, 6211-6224.
886 Pogge von Strandmann, P. A. E., Dohmen, R., Marschall, H. R., Schumacher, J. C. and Elliott, T.
887 (2015) Extreme Magnesium Isotope Fractionation at Outcrop Scale Records the
888 Mechanism and Rate at which Reaction Fronts Advance. J. Petrol. **56**, 33-58.
889 Pöml, P., Menneken, M., Stephan, T., Niedermeier, D. R. D., Geisler, T. and Putnis, A. (2007)
890 Mechanism of hydrothermal alteration of natural self-irradiated and synthetic crystalline
891 titanate-based pyrochlore. Geochim. Cosmochim. Acta **71**, 3311-3322.
892 Putnis, A. (2009) Mineral Replacement Reactions. Rev. Mineral. Geochem. **70**, 87-124.
893 Putnis, C. V., Tsukamoto, K. and Nashimura, Y. (2005) Direct observation for pseudomorphism:
894 Compositional and textural evolution at a solid-fluid interface. Am. Mineral. **90**, 1909-
895 1912.
896 Raufaste, C., Jamtveit, B., John, T., Meakin, P. and Dysthe, D. K. (2011) The mechanism of
897 porosity formation during solvent-mediated phase transformations. Proc. Math. Phys.
898 Eng. Sci. **467**, 1408-1426.
899 Roberts, J. A., Kenward, P. A., Fowle, D. A., Goldstein, R. H., González, L. A. and Moore, D. S.
900 (2013) Surface chemistry allows for abiotic precipitation of dolomite at low temperature.
901 PNAS **110,** 14540-14545.
902 Rosenberg, P. E. and Holland, H. D. (1964) Calcite-Dolomite-Magnesite Stability Relations in
903 Solutions at Elevated Temperatures. Science **145**, 700-701.
904 Rosenberg, P. E., Burt, D. M. and Holland, H. D. (1967) Calcite-dolomite-magnesite stability
905 relations in solutions: the effect of ionic strength. Geochim. Cosmochim. Acta **81**, 391-
906 396.
907 Schöne, B. (2013) Arctica islandica (Bivalvia): A unique paleonvironmental archive of the
908 northern North Atlantic Ocean. Global Planet. Change **111,** 199-225.
909 Sibley, D. F. (1990) Unstable to stable transformations during dolomitization. Journal of Geology
910 **98**, 739-748.
911 Sibley, D. F., Nordeng, S. H. and Borkowski, M. L. (1994) Dolomitization kinetics in
912 hydrothermal bombs and natural settings. J. Sediment. Res. **A64**, 630-637.

913 Steefel, C. I., DePaolo, D. J. and Lichtner, P. C. (2005) Reactive transport modeling: An essential
914 tool and a new research approach for the Earth sciences. Earth Planet. Sci. Lett. **240**, 539-
915 558.
916 Schott, J., Mavromatis, V., Fujii, T., Pearce, C.R., and Oelkers, E.H. (2016). The control of
917 magnesium aqueous speciation on Mg isotope composition in carbonate minerals:
918 theoretical and experimental modeling. Chem. Geol.,
919 doi:10.1016/j.chemgeo.2016.03.011
920 Swart, P. K., 2015, The geochemistry of carbonate diagenesis: The past, present and future.
921 Sedimentology **62**, 1233-1304.
922 Sykes, G. A., Collins, M. J. and Walton, D. I. (1995) The significance of a geochemically
923 isolated intracrystalline organic fraction within biominerals. Org. Geochem. **23**, 1059-
924 1065.
925 Tipper, E .T., Galy, A. and Bickle, M. J. (2006) Riverine evidence for a fractionated reservoir of
926 Ca and Mg on the continents: Implications for the oceanic Ca cycle. Earth Planet. Sci.
927 Lett. **247,** 267-279.
928 Towe, K. M. and Thompson, G. R. (1972) The structure of some bivalve shell carbonates
929 prepared by ion beam thinning. Calcifying Tissue Research **10**, 38-48.

930 Tribble, J. S., Arvidson, R. S., Lane III, M. and Mackenzie, F. T. (1995) Crystal chemistry, and
931 thermodynamic and kinetic properties of calcite, dolomite, apatite, and biogenic silica:
932 applications to petrologic problems. Sediment. Geol. **95**, 11-37.

933 Vandeginste, V., John, C.M., Van de Flierdt, T. and Cosgrove, J.W. (2013) Linking process,
934 dimension, texture, and geochemistry in dolomite geobodies: A case study from Wadi
935 Mistal (northern Oman). AAPG Bull. **97,** 1181-1207.

936 Vasconcelos, C., McKenzie, J. A., Bernasconi, S., Grujic, D. and Tien, A. J. (1995) Microbial
937 mediation as a possible mechanism for natural dolomite formation at low temperatures.
938 Nature **377,** 220-222.

939 Wanless, H.R. (1979) Limestone response to stress: pressure solution and dolomitization. J.
940 Sediment. Petrol. **49,** 437-462.

941 Warren, J. (2000) Dolomite: occurrence, evolution and economically important associations.
942 Earth-Sci. Rev. **52,** 1-81.

943 Warthmann, R., Van Lith, Y., Vasconcelos, C., McKenzie, J. A. and Karpoff, A. M. (2000)
944 Bacterially induced dolomite precipitation in anoxic culture experiments. Geology **28,**
945 1091-1094.

946 Wenk, H. R. and Zenger, D. H. (1983) Sequential Basal Faults in Devonian Dolomite, Nopah
947 Range, Death Valley Area, California. Science **222**, 502-504.

948 Whitaker, F. F. and Xiao, Y. (2010) Reactive transport modeling of early burial dolomitization of
949 carbonate platforms by geothermal convection. AAPG Bull. **94**, 889-917.

950 Zempolich, W. G. and Baker, P. A. (1993) Experimental and natural mimic dolomitization of
951 aragonite ooids. J. Sediment. Petrol. **63**, 596-606.

952 Zhang, F.F., Xu, H.F., Konishi, H., Shelobolina, E.S., and Roden, E.E. (2012). Polysaccharide-
953 catalyzed nucleation and growth of disordered dolomite: A potential precursor of
954 sedimentary dolomite. Am. Miner. **97**, 556-567.

Table 1

Table 1: Summary of hydrothermal experiments conducted with different aragonitic starting materials.

Sample	Starting material	V_{Fluid} [ml]	t [days]	Weight before experiment [mg]	Weight after experiment [mg]	Δm [%]
K12*	Porites sp.	1	1	152.20	151.47	0.48
K16*		0.905	2	137.67	130.94	4.89
K17*		0.939	5	142.86	134.67	5.73
K18*		0.954	10	145.15	134.62	7.25
K19*		0.953	20	145.11	133.04	8.32
M1	Arctica Islandica	1	20	130.95	126.69	3.25
M4		1	20	140.11	133.51	4.71
A4	Single crystals	1	20	223.85	219.90	1.76
A5		1	20	224.81	222.27	1.13
A6		1	20	242.01	237.86	1.71

* Experimental time series conducted with a constant water-to-rock (w/r) ratio of 6.57.

Table 2

Table 2: Representative electron microprobe analysis of the starting materials and the respective product phases from each experimental setup.

		Oxides [wt.%]					Mole fraction				
		MgO	CaO	MnO	FeO	SrO	X_{Mg}	X_{Ca}	X_{Mn}	X_{Fe}	X_{Sr}
Single crystal	Unreacted aragonite	0.01	56.25	0.02	0.023	0.18	0.000	0.998	0.000	0.000	0.002
	Zone 1	44.88	2.10	0.00	0.01	0.10	0.966	0.033	0.000	0.000	0.001
	Zone 2	36.10	12.57	0.04	0.03	0.71	0.793	0.200	0.001	0.000	0.006
	Zone 3	14.49	38.94	0.00	0.09	0.20	0.340	0.657	0.000	0.001	0.002
	Zone 4	2.89	52.91	0.02	0.03	0.19	0.070	0.330	0.000	0.000	0.002
	Aragonite patches	0.01	56.20	0.00	0.09	0.05	0.000	0.998	0.000	0.001	0.001
A. islandica	Unreacted aragonite	1.96	53.18	0.02	0.01	0.13	0.051	0.947	0.000	0.000	0.001
	Zone 1	37.09	5.58	0.02	0.02	0.19	0.901	0.097	0.000	0.000	0.002
	Zone 2	18.28	30.16	0.01	0.02	0.12	0.457	0.541	0.000	0.000	0.001
	Zone 3	14.45	33.03	0.01	0.01	0.12	0.377	0.622	0.000	0.000	0.001
Porites sp.	Unreacted aragonite	0.19	55.38	0.02	0.02	0.99	0.005	0.985	0.000	0.000	0.010
	Zone 1	37.69-45.01	12.07-4.52	0.03-0.02	0.03-0.02	0.22-0.25	0.81-0.93	0.07-0.19	0.000	0.000	0.002
	Zone 2	17.43	35.34	0.02	0.02	0.31	0.406	0.591	0.000	0.000	0.003
	Zone 3	19.21	32.12	0.02	0.01	0.15	0.453	0.545	0.000	0.000	0.001

Note: The mole fractions were calculated for the mineral formulae of carbonate (MCO_3) based on M = (Ca + Mg + Mn + Fe + Sr) = 1

Table 3

Table 3: Measured fluid concentrations that reacted with coral fragments between one and 20 days using ICP-OES.

Sample	t [days]	Concentration [µg/g]					
		Mg	±σ	Ca	±σ	Sr	±σ
Starting solution		20470	120	2	0.1	1179	16
K12	1	13580	67	10144	75	1396	12
K16	2	8942	27	17055	81	1609	7
K17	5	7659	44	19155	158	1787	18
K18	10	7210	82	19698	96	1876	10
K19	20	8554	72	20614	181	1972	11

Note:The concentrations of Mnand Fe were measured, but proved to be below the detection limit.

Figure 1

Click here to download high resolution image

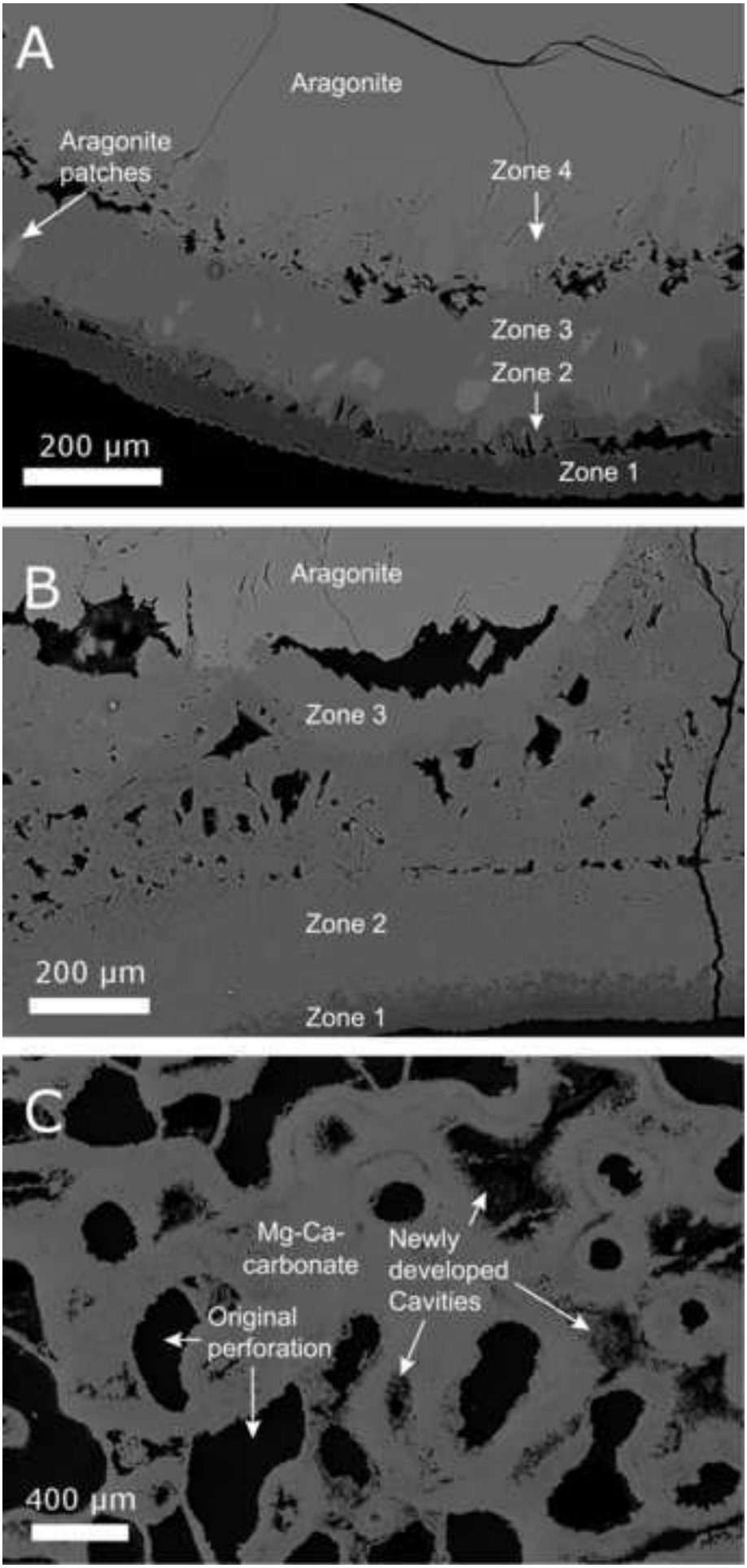

Figure 2

Click here to download high resolution image

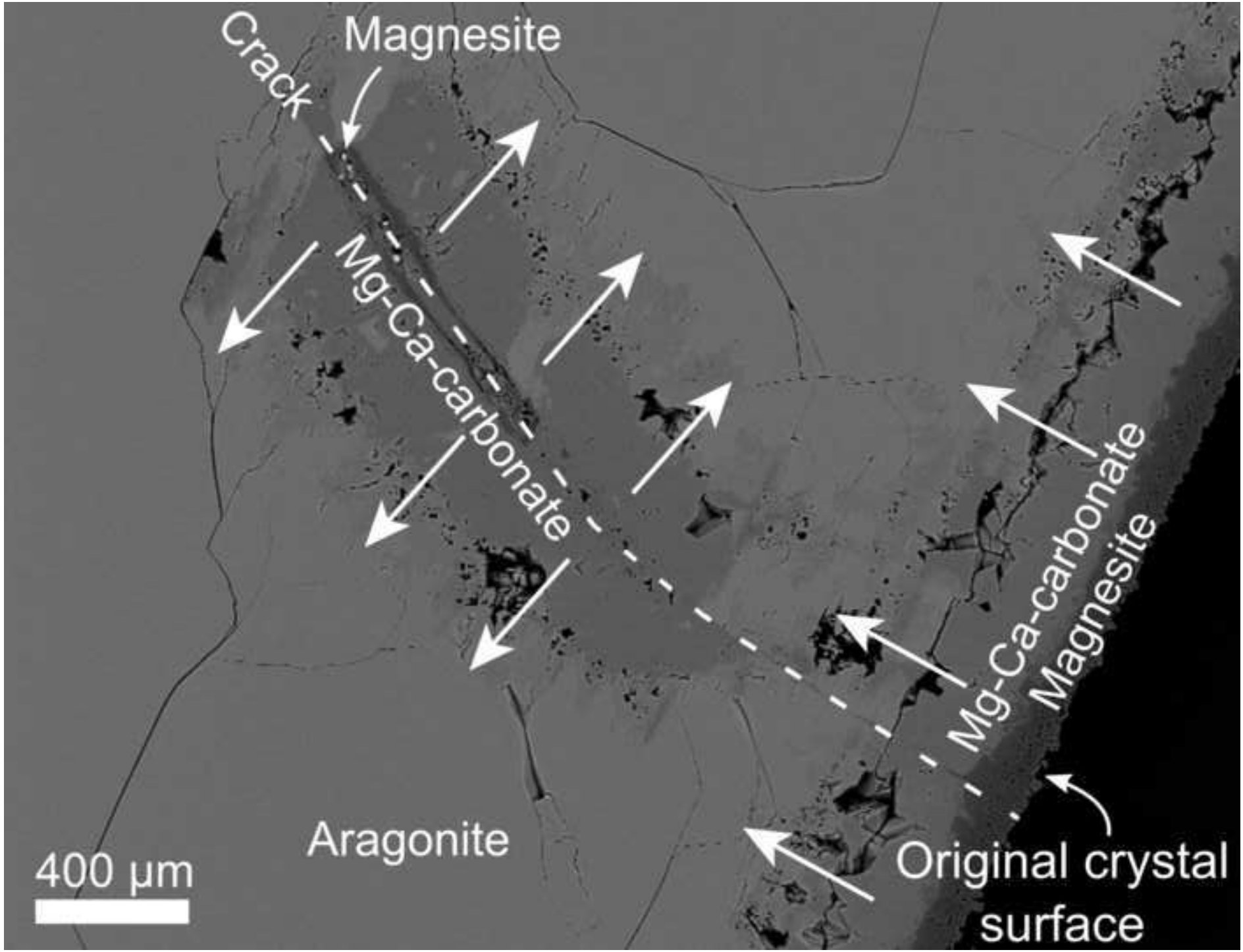

Figure 3

Click here to download high resolution image

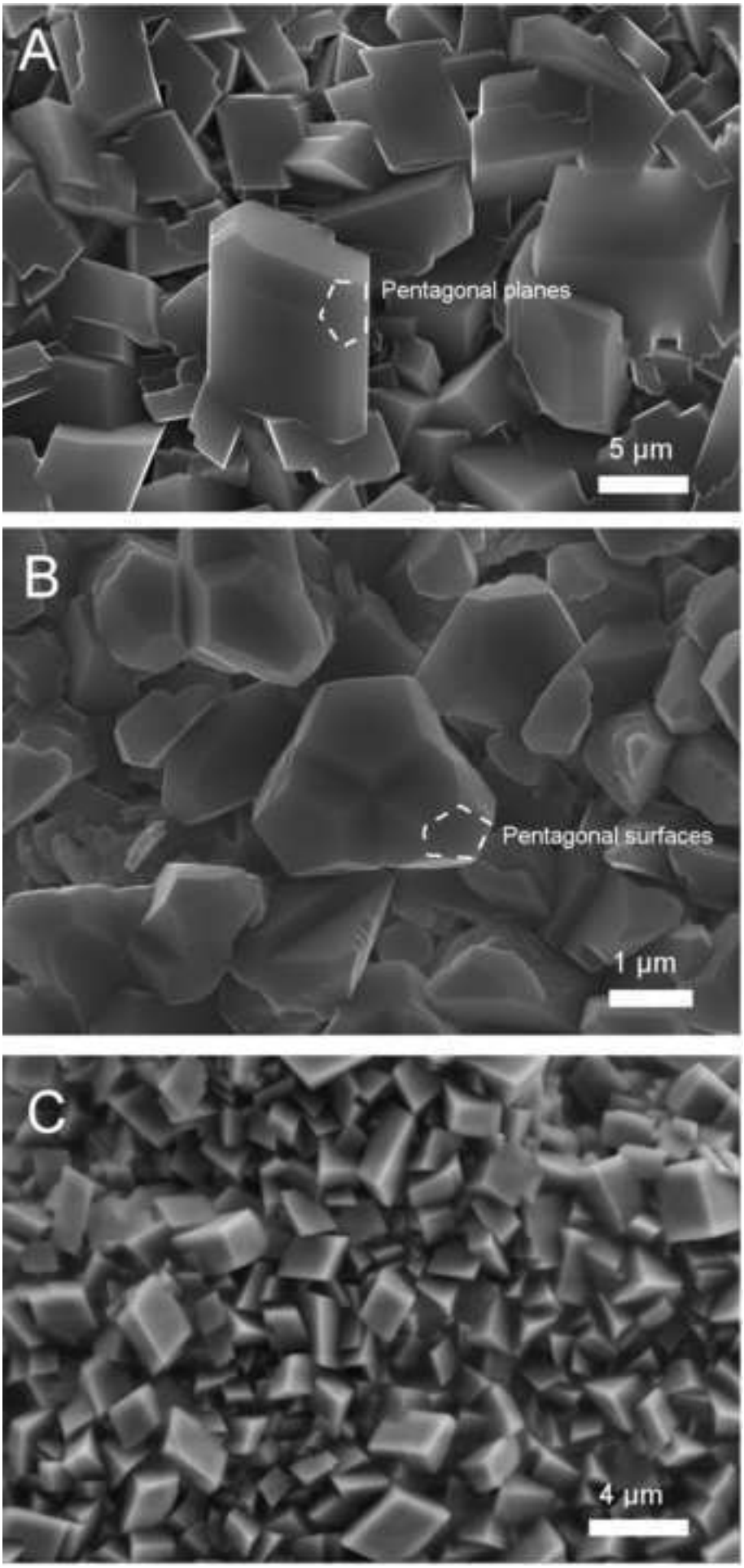

Figure 4

Click here to download high resolution image

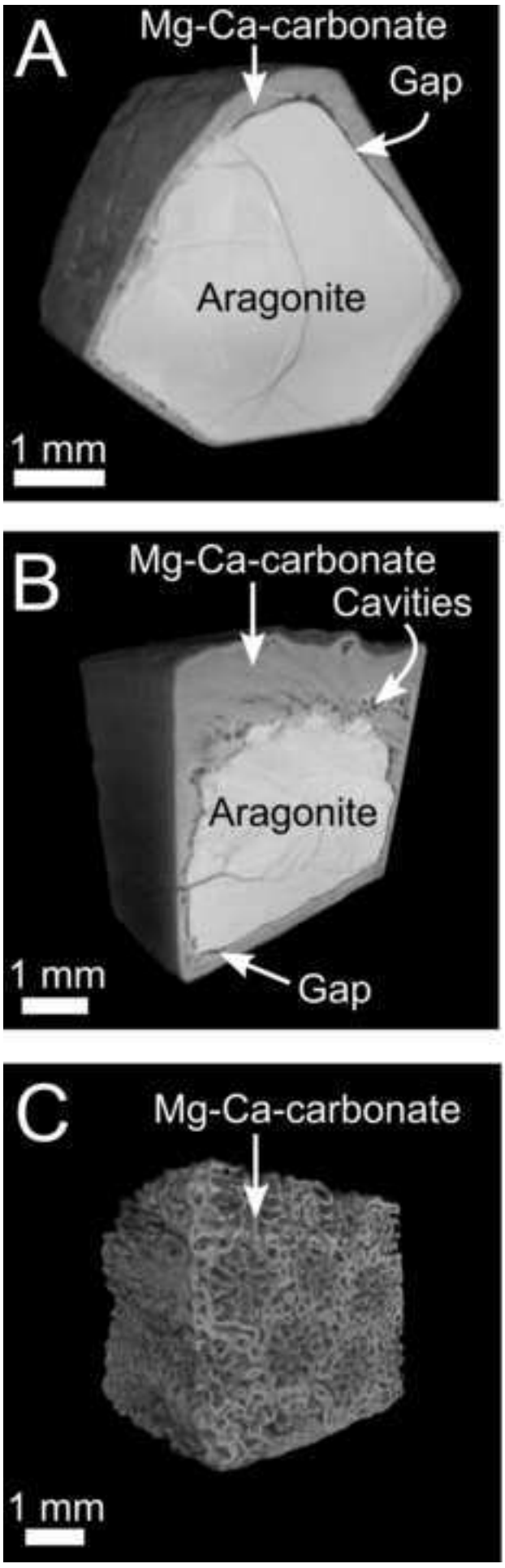

Figure 5

Click here to download high resolution image

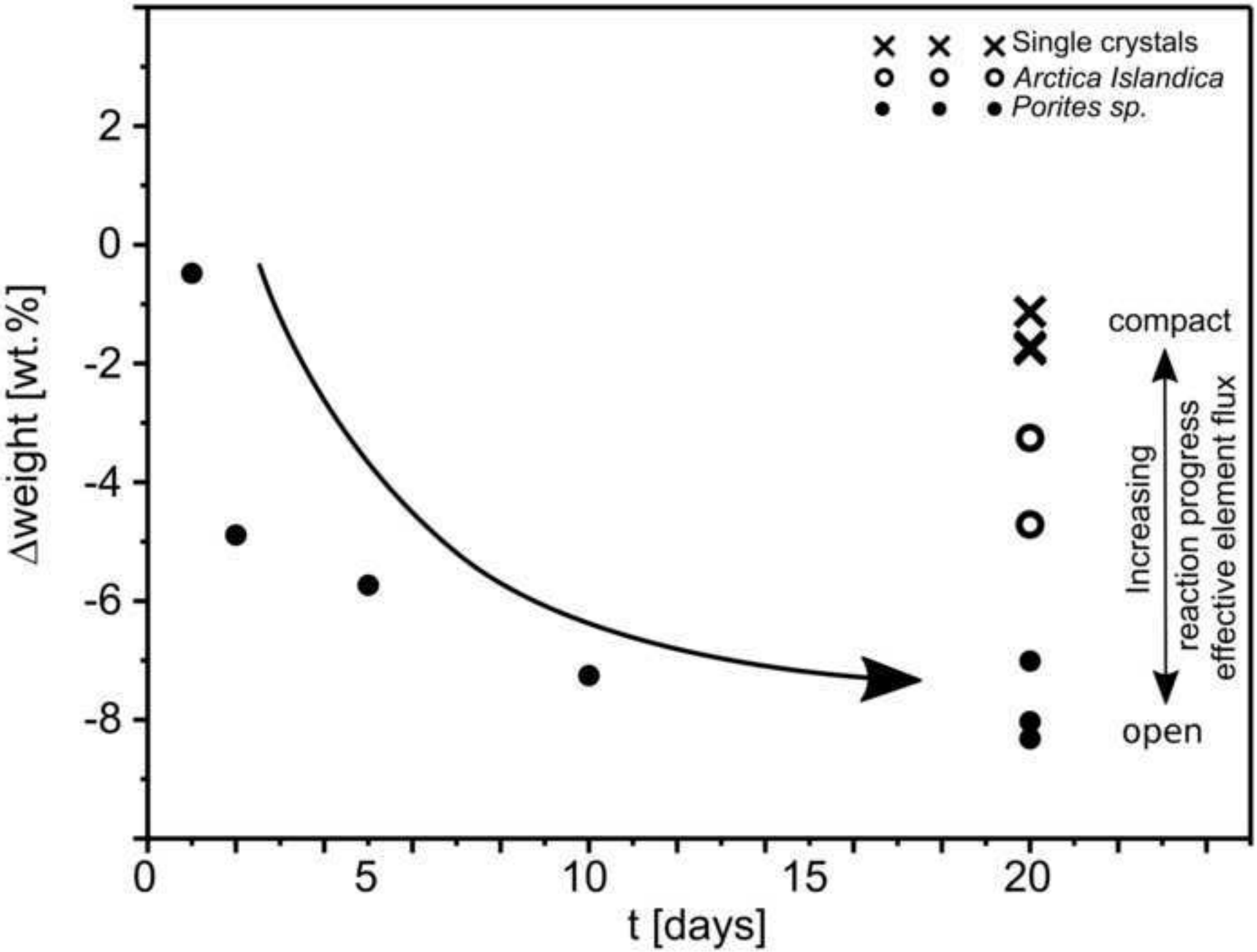

Figure 6

Click here to download high resolution image

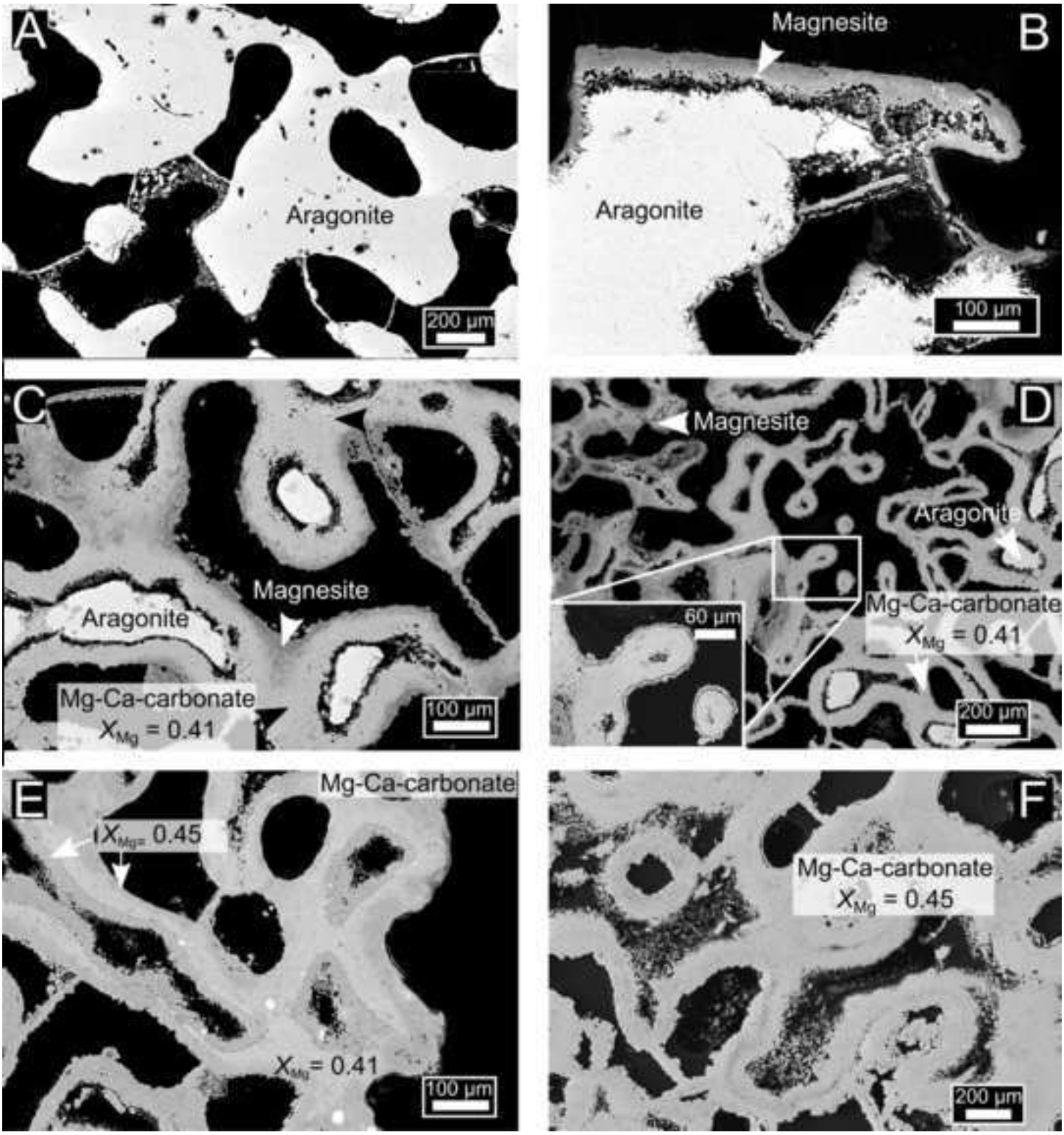

Figure 7

Click here to download high resolution image

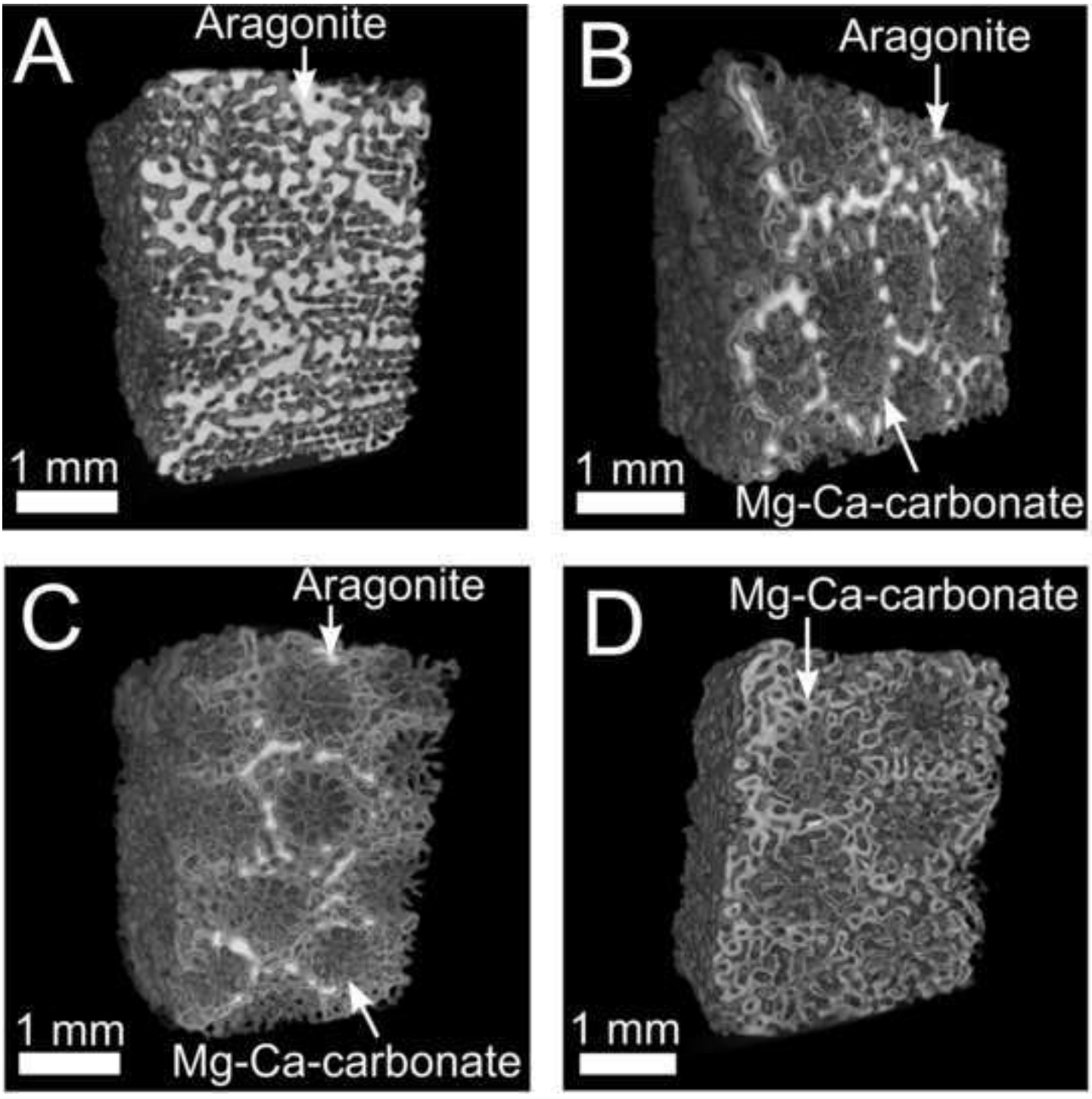

Figure 8

Click here to download high resolution image